



HAL
open science

Order from disorder phenomena in BaCoS₂

Benjamin Lenz, Michele Fabrizio, Michele Casula

► **To cite this version:**

Benjamin Lenz, Michele Fabrizio, Michele Casula. Order from disorder phenomena in BaCoS₂. Communications Physics, 2024, 7 (1), pp.35. 10.1038/s42005-023-01514-4 . hal-04397716

HAL Id: hal-04397716

<https://hal.science/hal-04397716>

Submitted on 16 Jan 2024

HAL is a multi-disciplinary open access archive for the deposit and dissemination of scientific research documents, whether they are published or not. The documents may come from teaching and research institutions in France or abroad, or from public or private research centers.

L'archive ouverte pluridisciplinaire **HAL**, est destinée au dépôt et à la diffusion de documents scientifiques de niveau recherche, publiés ou non, émanant des établissements d'enseignement et de recherche français ou étrangers, des laboratoires publics ou privés.

Order from disorder phenomena in BaCoS₂

Benjamin Lenz^{1*}, Michele Fabrizio² and Michele Casula¹

¹IMPMS, Sorbonne Université, CNRS, MNHN, 4 place Jussieu, Paris, F-75005, France.

²International School for Advanced Studies (SISSA), Via Bonomea 265, Trieste, I-34136, Italy.

*Corresponding author(s). E-mail(s):

benjamin.lenz@sorbonne-universite.fr;

Contributing authors: fabrizio@sissa.it;

michele.casula@sorbonne-universite.fr;

Abstract

At $T_N \simeq 300$ K the layered insulator BaCoS₂ transitions to a columnar antiferromagnet that signals non-negligible magnetic frustration despite the relatively high T_N , all the more surprising given its quasi two-dimensional structure. Here, we show, by combining *ab initio* and model calculations, that the magnetic transition is an order-from-disorder phenomenon, which not only drives the columnar magnetic order, but also the inter-layer coherence responsible for the finite Néel transition temperature. This uncommon ordering mechanism, actively contributed by orbital degrees of freedom, hints at an abundance of low energy excitations above and across the Néel transition, in agreement with experimental evidence.

1 Introduction

Frustrated magnets often display a continuous accidental degeneracy of the classical ground state that leads to the appearance of pseudo-Goldstone modes within the harmonic spin-wave approximation [1]. Since those modes are not protected by symmetry, they may acquire a mass once anharmonic terms are included in the spin-wave Hamiltonian. This mass, in turn, cuts off the singularities brought about by the pseudo-Goldstone modes, in that way stabilising ordered phases otherwise thwarted by fluctuations. To put it differently, let us imagine that the classical potential has

30 a manifold of degenerate minima generally not invariant under the symmetry group
 31 of the Hamiltonian. It follows that the eigenvalues of the Hessian of the potential
 32 change from minimum to minimum. Allowing for quantum or thermal fluctuations is
 33 therefore expected to favour the minima with lowest Hessian determinant, although
 34 the two kinds of fluctuations not necessarily select the same ones [2]. Moreover, it
 35 is reasonable to assume that the minima with lowest Hessian determinant are those
 36 that form subsets invariant under a symmetry transformation of the Hamiltonian so
 37 that choosing any of them corresponds to a spontaneous symmetry breaking. Such a
 38 phenomenon, also known as order from disorder [3], emerges in many different con-
 39 texts [4], from particle physics [5, 6] to condensed matter physics [7, 8], even though
 40 frustrated magnets still provide the largest variety of physical realisations [1–3, 9–15].

41
 42 The layered insulator BaCoS_2 might be legitimately included in the class of frus-
 43 trated magnets. Below a critical temperature T_N , BaCoS_2 becomes an antiferromagnet
 44 characterised by columnar spin-ordered planes, which we hereafter refer to as antifer-
 45 romagnetic striped (AFS) order, a classic symptom of frustration. The planes are in
 46 turn stacked ferromagnetically along the c -axis, so called C-type stacking as opposed
 47 to the antiferromagnetic G-type one. Inelastic neutron scattering (INS) experiments
 48 show that magnetic excitations below T_N have pronounced two-dimensional (2D)
 49 character [16, 17] implying strong quantum and thermal fluctuations that join with
 50 magnetic frustration to further hamper magnetic order. In spite of all that, the Néel
 51 temperature of BaCoS_2 is rather large, between 290 K [18] and 305 K [19], which is
 52 highly surprising. Indeed, a direct estimate of the spin exchange constants by neutron
 53 diffraction has been recently attempted in doped tetragonal $\text{BaCo}_{0.9}\text{Ni}_{0.1}\text{S}_{1.9}$ subject
 54 to an uniaxial strain [17]. This compound undergoes a Néel transition to the C-type
 55 AFS phase at 280 K [17], not far from T_N of undoped BaCoS_2 . The neutron data
 56 were fitted by a conventional $J_1 - J_2$ Heisenberg model [13] on each plane plus an
 57 inter-plane ferromagnetic exchange J_c , yielding $J_2 \sim 9.3$ meV, $J_1 \sim -2.3$ meV and
 58 $0 < |J_c| < 0.04$ meV, with the upper bound due to experimental resolution. The Néel
 59 temperature can be overestimated discarding J_1 [20] and taking $|J_c|$ equal to the upper
 60 bound. In that way, one obtains [21] $T_N \simeq 200$ K, which, despite supposedly being an
 61 overestimate, is 2/3 smaller than the observed value. This discrepancy is puzzling.

62 Another startling property is the anomalously broad peak of the magnetic suscepti-
 63 bility at T_N [18, 19], which suggests a transition in the Ising universality class rather
 64 than the expected Heisenberg one [19]. A possible reason of this behaviour might be
 65 spin-orbit coupling [19]. Indeed, a Rashba effect due to the layered structure and
 66 the staggered sulfur pyramid orientation, see Fig. 1, has been found to yield sizeable
 67 band splittings at specific points within the Brillouin zone, at least in metallic tetrag-
 68 onal BaNiS_2 [22]. The Rashba-like spin-orbit coupling strength may barely differ in
 69 BaCoS_2 , or be weakened by strong correlations [23]. In either case, its main effect is
 70 to introduce an easy plane anisotropy, as indeed observed experimentally [19], which,
 71 at most, drives the transition towards the XY universality class. It is well possible
 72 that the weak orthorhombic distortion in BaCoS_2 may turn the easy plane into an
 73 easy axis, but the resulting magnetic anisotropy should be negligibly small and thus
 74 unable to convincingly explain the experimental observations.

75 Lastly, BaCoS₂ shows a very strange semiconducting behaviour above T_N , with acti-
 76 vated dc conductivity, no evidence of a Drude peak and, yet, an optical conductivity
 77 that grows linearly in frequency [24].

78
 79 The relatively high T_N despite magnetic frustration and quasi-two dimensional
 80 character, as well as the abundance of low energy excitations above and across the
 81 Néel transition are pieces of evidence that some kind of order-from-disorder phe-
 82 nomenon takes place in BaCoS₂, a scenario that we here support by a thorough
 83 analysis combining *ab initio* and model calculations.

85 2 Results

86 2.1 Phase diagram of BaCoS₂

87 BaCoS₂ is a metastable layered compound that, quenched from high temperature,
 88 crystallises in an orthorhombic structure with space group $Cmme$, no. 67 [25], charac-
 89 terised by in-plane primitive lattice vectors $a \neq b$. However, we believe physically more
 90 significant to consider as reference structure the higher-symmetry non-symmorphic
 91 $P4/nmm$ tetragonal one ($a = b$) of the opposite end member, BaNiS₂, and regard
 92 the orthorhombic distortion as an instability driven by the substitution of Ni with
 93 the more correlated Co. The hypothetical tetragonal phase of BaCoS₂ is shown in
 94 Fig. 1(A). Each CoS $a - b$ plane has two inequivalent cobalt atoms, Co(1) and Co(2),
 95 see Fig. 1(B), which are related to each other by a non-symmorphic symmetry.

96 Below T_N , an AFS magnetically ordered phase sets in. In the $a - b$ plane it consists of
 97 ferromagnetic chains, either along a (AFS-a) or b (AFS-b), coupled antiferromagnet-
 98 ically, see Fig. 1(C). The stacking between the planes is C-type, i.e., ferromagnetic,
 99 thus the labels C-AFS-a and C-AFS-b that we shall use, as well as G-AFS-a and
 100 G-AFS-b whenever we discuss the G-type configurations with antiferromagnetic stack-
 101 ing. We mention that the orthorhombic distortion with $b > a$ ($a > b$) is associated
 102 with C-AFS-a (C-AFS-b), i.e., ferromagnetic bonds along a (b) [19], at odds with the
 103 expectation that ferromagnetic bonds are longer than antiferromagnetic ones. This
 104 counterintuitive behaviour represents a key test for the *ab initio* calculations that we
 105 later present.

106 Neutron scattering refinement and magnetic structure modelling in the low-
 107 temperature phase point to an ordered moment of $\mu_{Co} \sim 2.63 - 2.9\mu_B$ [19, 26],
 108 suggesting that each Co²⁺ is in a $S = 3/2$ spin configuration, in agreement with
 109 the high-temperature magnetic susceptibility [19]. Moreover, the form factor analysis
 110 of the neutron diffraction data [26] indicates that the three 1/2-spins lie one in the
 111 $d_{3z^2-r^2}$, the other in the $d_{x^2-y^2}$, and the third either in the d_{xz} or d_{yz} 3d-orbitals of
 112 Co. Since d_{xz} and d_{yz} , which we hereafter denote shortly as x and y orbitals, form in
 113 the $P4/nmm$ tetragonal structure a degenerate E_g doublet occupied by a single hole,
 114 such degeneracy is going to be lifted at low-temperature. That hints at the existence of
 115 some kind of orbital order, besides the spin one, in the magnetic orthorhombic phase.

116 Let us try to anticipate by symmetry arguments which kind of order can be stabilised.

117 We observe that in the $Cmme$ orthorhombic structure the cobalt atoms occupy

118 the Wyckoff positions $4g$, which, for convenience, we denote as $\text{Co}(1) \equiv (0, 0, z)$,
 119 $\text{Co}(2) \equiv (1/2, 0, -z)$, $\text{Co}(3) \equiv (0, 1/2, -z)$, $\text{Co}(4) \equiv (1/2, 1/2, z)$, and have symme-
 120 try $mm2$. As a consequence, the hole must occupy either the x orbital or the y one,
 121 but not a linear combination, and the chosen orbital must be the same for $\text{Co}(1)$ and
 122 $\text{Co}(4)$, as well as for $\text{Co}(2)$ and $\text{Co}(3)$. Therefore, we denote as d_n , $d = x, y$, the orbital
 123 occupied by the hole on $\text{Co}(n)$, $n = 1, \dots, 4$, and as $d_1d_2d_3d_4$ a generic orbital con-
 124 figuration. Then, there are only four of them that are symmetry-allowed: $xxxx$, $yyyy$,
 125 $xyyx$ and $yxyx$, see Fig. 2.

126 We remark that $xxxx$ is degenerate with $yyyy$ in the tetragonal phase. The choice of
 127 either of them is associated with the same $C_4 \rightarrow C_2$ symmetry breaking that charac-
 128 terises both the AFS-a or AFS-b spin order and the orthorhombic distortion, $b > a$ or
 129 $a > b$. All these three choices can be associated with three Ising variables τ , σ and X
 130 such that $\tau = +1$ corresponds to $xxxx$, $\sigma = +1$ to AFS-a, $X = +1$ to $b > a$, and vice
 131 versa. Since they all have the same symmetry, odd under C_4 , they would be coupled
 132 to each other should we describe the transition by a Landau-Ginzburg functional. We
 133 shall hereafter denote as $Z_2(C_4)$ the Ising sector that describes the $C_4 \rightarrow C_2$ symme-
 134 try breaking.

135 The other two allowed orbital configurations $xyyx$ and $yxyx$ (see Fig. 2) are instead
 136 degenerate both in the tetragonal and orthorhombic phases, but break the non-
 137 symmorphic symmetry (NS) that connects, e.g., $\text{Co}(1)$ with $\text{Co}(2)$ and $\text{Co}(3)$. We can
 138 therefore associate to those configurations a new Ising sector $Z_2(\text{NS})$.

139 We emphasise that the above conclusions rely on the assumption of a $Cmme$
 140 space group. A mixing between x and y orbitals is instead allowed by the $Pba2$ space
 141 group proposed in Ref. [27] as an alternative scenario for BaCoS_2 at room temper-
 142 ature. As a matter of fact, the two symmetry-lowering routes, $P4/nmm \rightarrow Cmme$
 143 and $P4/nmm \rightarrow Pba2$, correspond to different Jahn-Teller-like distortions involving
 144 the d_{xz} - d_{yz} doublet and the E_g phonon mode of the $P4/nmm$ structure at the \mathbf{M}
 145 point, which is found to have imaginary frequency by *ab initio* calculations [27]. How-
 146 ever, latest high-accuracy X-ray diffraction data [18] confirm the $Cmme$ orthorhombic
 147 structure even at room temperature, thus supporting our assumption.

148 2.2 *Ab initio* analysis

149 Using density functional theory (DFT) and DFT+U calculations, in the first place,
 150 we checked if the tetragonal phase is unstable towards magnetism, considering both a
 151 conventional Néel order (AFM) compatible with the bipartite lattice and the observed
 152 AFS. We found, using a Hubbard interaction of $U = 2.8$ eV and a Hund's coupling
 153 constant $J = 0.95$ eV for the Co-3d orbitals as motivated by constrained random
 154 phase approximation (cRPA) [24], that the lowest energy state is indeed the AFS, the
 155 AFM and non-magnetic phases lying above by about 0.5 eV and 2.3 eV, respectively.
 156 Let us therefore restrict our analysis to AFS and stick to $U = 2.8$ eV. Note, however,
 157 that the ordering of the four configurations with lowest energy within our DFT+U
 158 simulations does not change within 2 eV around that value. The main assumptions
 159 entering our *ab initio* modelling are thereby not sensitive to the precise choice of U
 160 around the value motivated by cRPA calculations. We use an 8-site unit cell that
 161 includes two planes, which allows us to compare C-AFS with G-AFS. In addition, we

162 consider both the tetragonal structure with AFS-a, since AFS-b is degenerate, and
 163 the orthorhombic structure with $b > a$, in which case we analyse both AFS-a and
 164 AFS-b. For all cases, we investigate all four symmetry-allowed orbital configurations,
 165 $xxxx$, $yyyy$, $xyyx$ and $yxyx$, assuming either a C-type or G-type orbital stacking
 166 between the two planes of the unit cell, so that, for instance, $G(xxxx)$ means that
 167 one plane is in the $xxxx$ configuration and the other in the $yyyy$ one.

168
 169 In Table 1 we report the energies per formula unit of several possible configurations
 170 in the tetragonal structure, including those that would be forbidden in the orthorhom-
 171 bic one. All energies are measured with respect to the lowest energy state and are
 172 expressed in Kelvin. In agreement with experiments, the lowest energy state T0 has
 173 spin order C-AFS, a or b being degenerate. In addition, it has C-type antiferro-orbital
 174 order, $C(xyxx)$. We note that its G-type spin counterpart T1 is only 2 K above, sup-
 175 porting our observation that $T_N = 290$ K is anomalously large if compared to these
 176 magnetic excitations. The abundance of nearly degenerate ground states is consistent
 177 with the seminal DFT+U study by Zainullina and Korotin [28], where the importance
 178 of different orbital configurations for a given stripe magnetic phase was studied for a
 179 larger value of U .

180 The energy differences between C-type orbital stacked configurations and their G-type
 181 counterparts are too small to allow obtaining a reliable modelling of the inter-plane
 182 orbital coupling. On the contrary, the energy differences between in-plane orbital con-
 183 figurations can be accurately reproduced by a rather simple modelling. We assume on
 184 each Co-site an Ising variable τ_3 equal to the difference between the hole occupations
 185 of orbital x and of orbital y . The Ising variable on a given site is coupled only to
 186 those of the four nearest neighbour sites in the $a - b$ plane, with exchange constants
 187 $\Gamma_{1a} = \Gamma_1 + \sigma \delta\Gamma_1$ and $\Gamma_{1b} = \Gamma_1 - \sigma \delta\Gamma_1$ along a and b , respectively. In addition, the
 188 Ising variables feel a uniform field $B_\tau \sigma$. Here, σ is the Ising $Z_2(C_4)$ order parameter
 189 that distinguishes AFS-a, $\sigma = +1$ from AFS-b, $\sigma = -1$. We find that the spectrum is
 190 well reproduced by the parameters in Table 2. It is worth noticing that the in-plane
 191 antiferro-orbital order is unexpected in light of the nematic columnar spin order that
 192 would rather suggest the ferro-orbital $xxxx$ or $yyyy$ configurations to have lowest
 193 energy. The explanation is that the antiferro-orbital order yields within DFT+U a
 194 larger insulating gap than the ferro-orbital order, see Fig.3.

195
 196 We now move to the physical orthorhombic structure, assuming $b > a$ with
 197 $b/a = 1.008$ [25], and recalculate all above energies but considering only the orbital
 198 configurations allowed by the $Cmme$ space group. In this case, we have to distinguish
 199 between AFS-a and AFS-b, which are no longer degenerate. The results are shown in
 200 Table 3.

201 The calculated magnetic moment per Co atom in the lowest energy state, O0 in
 202 Table 3, is $\mu_{AFS} \sim 2.65 \mu_B$, in quite good agreement with experiments [19, 26]. We
 203 remark that the *ab initio* calculation correctly predicts that the lowest energy state O0
 204 has ferromagnetic bonds along a despite $b > a$, which, as we mentioned, is an impor-
 205 tant test for the theory. The energy difference between AFS-a and AFS-b, i.e., O0 and
 206 O3, is about 20 K, and gives a measure of the spin-exchange spatial anisotropy in the

207 a and b directions due to the orthorhombic distortion. This small value implies that
 208 the Néel transition temperature $T_N \simeq 290$ K is largely insensitive to the orthorhombic
 209 distortion that exists also above T_N [18, 19]. In particular, the energy difference
 210 between C-type and G-type stacking, O0 and O1 in Table 3, remains the same tiny
 211 value found in the tetragonal phase. Table 3 thus suggests that the spin configurations
 212 C-AFS-a, C-AFS-b, G-AFS-a and G-AFS-b are almost equally probable at the Néel
 213 transition, and that despite the orthorhombic structure.

214 The orbital arrangement of the C-AFS-a configuration is also important to describe,
 215 e.g., the pressure-induced metal-insulator transition in BaCoS₂, see Supplementary
 216 Note 1.

217 2.2.1 Orthorhombic distortion.

218 A further evidence of the marginal role played by the orthorhombic distortion at
 219 the Néel transition comes from the total energy as function of the parameter $d =$
 220 $2(a-b)/(a+b)$ that quantifies the distortion, shown in Fig. 4 for different orbital con-
 221 figurations assuming AFS-a magnetic order. We note that for all orbital configurations
 222 the energy gain due to a finite d is tiny with respect to $d = 0$. For instance, the lowest-
 223 energy orbital configuration $xyyx$ reaches a minimum at about $d_{\min}^{xyyx} \sim -0.5\%$, not
 224 far from the experimental value $d_{\text{exp}} \sim -0.8\%$ [25], which reduces to $d_{\text{exp}} \sim -0.4\%$
 225 under high pressure synthesis [18]. However, the energy gain with respect to $d = 0$ is
 226 less than 3 K. This result suggests that, despite the hypothetical $P4/nmm$ structure
 227 of BaCoS₂ being inherently unstable to an orthorhombic Jahn-Teller distortion, the
 228 latter plays almost no role in stabilising the AFS magnetic order in contrast to naïve
 229 expectations.

230 2.2.2 Wannierisation

231 To gain further insight into the mechanisms that drive the Néel transition, we generate
 232 two tight-binding Hamiltonians with maximally-localised Wannier functions for Co-
 233 d -like and Co- d_{xz}/d_{yz} -like orbitals, respectively. Both tight-binding models reproduce
 234 overall well the DFT band structure of the PM phase in the orthorhombic structure,
 235 see Fig. 5. Whereas the fit of the 5-orbital model is nearly perfect, the 2-orbital model
 236 shows small deviations along the $\mathbf{M} - \Gamma$ direction due to missing hybridisation with
 237 the other Co- d orbitals. Table 4 shows the leading hopping processes of the 5-band
 238 model restricted to the (d_{xz}, d_{yz}) subspace.

239 We note that, because of the staggered shift of the Co atoms out of the sulfur basal
 240 plane, the largest intra-layer hopping is between next-nearest neighbour (NNN) cobalt
 241 atoms instead of nearest-neighbour (NN) ones. Moreover, the stacking of the sulfur
 242 pyramids and the position of the intercalated Ba atoms makes the inter-layer NN
 243 hopping negligible, contrary to the NNN one that is actually larger than the in-plane
 244 NN hopping, but still smaller than the in-plane NNN one ($t_{NN}^{\text{inter}} \ll t_{NN}^{\text{intra}} < t_{NNN}^{\text{inter}} <$
 245 t_{NNN}^{intra}).

246 We finally remark that the orthorhombic distortion has a very weak effect on the inter-
 247 layer hopping, which is consistent with the tiny energy difference between C-AFS and
 248 G-AFS being insensitive to the distortion, compare, e.g., the energies of T1 and O1
 249 in Tables 1 and 3, respectively.

2.3 Effective Heisenberg model

Armed with all the above *ab initio* results, we are now ready to address the main questions of this work, i.e., why T_N is so high and why the Néel transition looks Ising-like.

We already mentioned that the largest energy scales that emerge from the *ab initio* calculations are the magnetic ones separating the lowest-energy AFS configuration from the Néel and non-magnetic states. Therefore, even though BaCoS₂ seems not to lie deep inside a Mott insulating regime, we think it is worth discussing qualitatively the spin dynamics in terms of an effective $S = 3/2$ Heisenberg model. If we assume that the leading contribution to the exchange constants derives from the hopping processes within the $d_{xz} - d_{yz}$ subspace, then Table 4 suggests the Heisenberg model shown in Fig. 6. According to this figure, the exchange constants $J_{1x/y}$, J_2 , and $J_{3x/y}$ are related to the hopping terms $T_{(\pm 1, 0, 0)/(0, \pm 1, 0)}$, $T_{\pm(1, -1, 0)/\pm(1, 1, 0)}$, and $T_{(\pm 1, 0, 1)/(0, \pm 1, 1)}$, reported in Table 4. This model consists of frustrated $J_1 - J_2$ planes [13, 29–32] coupled to each other by a still frustrating J_3 coupling, see Fig. 6(b). In order to be consistent with the observed columnar magnetic order, the exchange constants have to satisfy the inequality $2J_2 > |J_3| + |J_1|$. Moreover, J_3 forces to deal with a two sites unit cell, highlighted in yellow colour in Fig. 6(a) where the non-equivalent cobalt sites are referred to as Co(1), in blue, and Co(2), in red, respectively. The reason is that Co(1) on a plane is only coupled to Co(2) on the plane above but not below, and vice versa for Co(2).

To simplify the notation, we write, for $a = 1, 3$, $J_{ax} = J_a(1 - \delta_a)$ and $J_{ay} = J_a(1 + \delta_a)$, where, in analogy with the single-layer $J_1 - J_2$ model [13], $\delta_a \neq 0$ are Ising order parameters associated with the $C_4 \rightarrow C_2$ symmetry breaking. Moreover, we define the in-plane Fourier transforms of the spin operators

$$\mathbf{S}_{\ell, n}(\mathbf{q}) = \sum_{\mathbf{R}} e^{-i\mathbf{q} \cdot \mathbf{R}} \mathbf{S}_{\ell, n, \mathbf{R}}, \quad (1)$$

where \mathbf{R} labels the N unit cells in the $a - b$ plane, $\ell = 1, 2$ the two sites (sublattices) within each unit cell, and $n = 1, \dots, L$ the layer index. With those definitions, the Hamiltonian reads

$$\begin{aligned} H = \frac{1}{N} \sum_{n\mathbf{q}} \left\{ J_2(\mathbf{q}) \left(\mathbf{S}_{1, n}(\mathbf{q}) \cdot \mathbf{S}_{1, n}(-\mathbf{q}) + \mathbf{S}_{2, n}(\mathbf{q}) \cdot \mathbf{S}_{2, n}(-\mathbf{q}) \right) \right. \\ \left. + J_1 \left(\gamma(\mathbf{q}, \delta_1) \mathbf{S}_{1, n}(\mathbf{q}) \cdot \mathbf{S}_{2, n}(-\mathbf{q}) + H.c. \right) \right. \\ \left. + J_3 \left(\gamma(\mathbf{q}, \delta_3) \mathbf{S}_{1, n}(\mathbf{q}) \cdot \mathbf{S}_{2, n+1}(-\mathbf{q}) + H.c. \right) \right\} \\ \equiv H_2 + H_1 + H_3, \end{aligned} \quad (2)$$

where H_a is proportional to J_a , $a = 1, 2, 3$, and

$$\begin{aligned} J_2(\mathbf{q}) &= 2J_2 \cos q_x \cos q_y, \\ \gamma(\mathbf{q}, \delta) &= e^{iq_x} \left[(1 - \delta) \cos q_x + (1 + \delta) \cos q_y \right]. \end{aligned} \quad (3)$$

The classical ground state corresponds to the three-dimensional modulation wave vector $(\pi, 0, Q_z) \equiv (0, \pi, Q_z)$, which describes an antiferromagnetic order within each sublattice on each layer, and where the inter-plane Q_z is the value that minimises the

282 classical energy per site, $E(Q_z) = -2J_2 - 2\sqrt{J_1^2\delta_1^2 + J_3^2\delta_3^2 + 2J_1J_3\delta_1\delta_3\cos Q_z}$. The
 283 expression of $E(Q_z)$ shows that inter-layer magnetic coherence sets in only when the
 284 two Ising-like order parameters, δ_1 and δ_3 , lock together. Specifically, $J_1J_3\delta_1\delta_3 > 0$
 285 stabilises C-AFS, $Q_z = 0$, otherwise G-AFS, $Q_z = \pi$. We already know that the
 286 former is lower in energy, though by only few Kelvins, see Table 3. Moreover, an
 287 orthorhombic distortion $b > a$ favours AFS-a, which implies $J_1\delta_1 + J_3\delta_3 > 0$, even
 288 though AFS-b is higher by only 20 K according to DFT+U, see O3 in Table 3.

289
 290 Using our $J_1 - J_2 - J_3$ model to fit the INS data of [17] at 200 K, we estimate $J_2 \simeq 9.3$
 291 meV, $J_1 + J_3 \simeq -2.34$ meV, $J_1\delta_1 + J_3\delta_3 \simeq 0.53$ meV, and $0 < \sqrt{J_1J_3\delta_1\delta_3} < 0.14$ meV,
 292 where, we recall, the upper bound is due to experimental resolution. Such small bound
 293 suggests that the two order parameters δ_1 and δ_3 are already formed at 200 K, whereas
 294 their mutual locking is still suffering from fluctuations. We finally observe that the
 295 ferromagnetic sign of J_1 and J_3 is consistent with the diagonal hopping matrices in the
 296 corresponding directions (see Table 4) and the antiferro-orbital order. Estimations of
 297 the exchange constants based on the DFT+U energies can be found in Supplementary
 298 Note 2.

300 2.3.1 Spin-wave analysis of the C_4 symmetric model

301 To better understand the interplay between the Z_2 (C_4) Ising degrees of freedom and
 302 the magnetic order at T_N , we investigate in more detail the Hamiltonian (2) with
 303 $\delta_1 = \delta_3 = 0$, thus $J_{1x} = J_{1y} = J_1$ and $J_{3x} = J_{3y} = J_3$. Since $J_2 > 0$ is the dominant
 304 exchange process, the classical ground state corresponds to the spin configuration

$$\mathbf{S}_{i,n}(\mathbf{q}) = NS \mathbf{n}_{3,i,n} \delta_{\mathbf{q},\mathbf{Q}}, \quad i = 1, 2, \quad n = 1, \dots, L, \quad (4)$$

305 where $S = 3/2$ is the spin magnitude, $\mathbf{n}_{3,i,n}$ is a unit vector, and $\mathbf{Q} = (\pi, 0) \equiv (0, \pi)$,
 306 the equivalence holding since $\mathbf{G} = (\pi, \pi)$ is a primitive in-plane lattice vector for the
 307 two-site unit cell. In other words, each sublattice on each plane is Néel ordered, and
 308 its staggered magnetisation $\mathbf{n}_{3,i,n}$ is arbitrary. We therefore expect that quantum and
 309 thermal fluctuations may yield a standard order-from-disorder phenomenon [3].

310 Within spin-wave approximation, the spin operators can be written as

$$\begin{aligned} \mathbf{S}_{i,n}(\mathbf{q}) \cdot \mathbf{n}_{3,i,n} &\simeq NS \delta_{\mathbf{q},\mathbf{Q}} - \Pi_{i,n}(\mathbf{q} - \mathbf{Q}), \\ \mathbf{S}_{i,n}(\mathbf{q}) \cdot \mathbf{n}_{1,i,n} &\simeq \sqrt{NS} x_{i,n}(\mathbf{q}), \\ \mathbf{S}_{i,n}(\mathbf{q}) \cdot \mathbf{n}_{2,i,n} &\simeq \sqrt{NS} p_{i,n}(\mathbf{q} - \mathbf{Q}), \end{aligned} \quad (5)$$

311 where $\mathbf{n}_{1,i,n}$, $\mathbf{n}_{2,i,n}$ and $\mathbf{n}_{3,i,n}$ are orthogonal unit vectors, $x_{i,n}^\dagger(\mathbf{q}) = x_{i,n}(-\mathbf{q})$ and
 312 $p_{i,n}^\dagger(\mathbf{q}) = p_{i,n}(-\mathbf{q})$ are conjugate variables, i.e.,

$$\left[x_{i,n}(\mathbf{q}), p_{j,m}^\dagger(\mathbf{q}') \right] = i \delta_{i,j} \delta_{n,m} \delta_{\mathbf{q},\mathbf{q}'}, \quad (6)$$

313 and

$$\begin{aligned} \Pi_{i,n}(\mathbf{q} - \mathbf{Q}) &= \frac{1}{2} \sum_{\mathbf{k}} \left(x_{i,n}^\dagger(\mathbf{k}) x_{i,n}(\mathbf{k} + \mathbf{q} - \mathbf{Q}) \right. \\ &\quad \left. + p_{i,n}^\dagger(\mathbf{k}) p_{i,n}(\mathbf{k} + \mathbf{q} - \mathbf{Q}) - \delta_{\mathbf{q},\mathbf{Q}} \right). \end{aligned} \quad (7)$$

314 The three terms of the Hamiltonian (2) thus read, at leading order in quantum
 315 fluctuations, i.e., in the harmonic approximation,

$$\begin{aligned}
 H_2 &\simeq E_0 + S \sum_{i, \mathbf{n}, \mathbf{q}} \left(J_2(\mathbf{q}) - J_2(\mathbf{Q}) \right) \left(x_{i,n}^\dagger(\mathbf{q}) x_{i,n}(\mathbf{q}) \right. \\
 &\quad \left. + p_{i,n}^\dagger(\mathbf{q} - \mathbf{Q}) p_{i,n}(\mathbf{q} - \mathbf{Q}) \right), \\
 H_1 &\simeq S J_1 \sum_{n, \mathbf{q}} \left(\gamma(\mathbf{q}) \mathbf{X}_{1,n}(\mathbf{q}) \cdot \mathbf{X}_{2,n}(-\mathbf{q}) + H.c. \right), \\
 H_3 &\simeq S J_3 \sum_{n, \mathbf{q}} \left(\gamma(\mathbf{q}) \mathbf{X}_{1,n}(\mathbf{q}) \cdot \mathbf{X}_{2,n+1}(-\mathbf{q}) + H.c. \right),
 \end{aligned} \tag{8}$$

316 where $E_0 = 2NL S(S+1) J_2(\mathbf{Q})$, $\gamma(\mathbf{q}) = \gamma(\mathbf{q}, \delta = 0)$, and

$$\mathbf{X}_{i,n}(\mathbf{q}) = \mathbf{n}_{1,i,n} x_{i,n}(\mathbf{q}) + \mathbf{n}_{2,i,n} p_{i,n}(\mathbf{q} - \mathbf{Q}). \tag{9}$$

317 We note that H_2 does not depend on the choice of $\mathbf{n}_{3,i,n}$, reflecting the classical acci-
 318 dental degeneracy, unlike $H_1 + H_3$. We start treating H_1 and H_3 within perturbation
 319 theory. The unperturbed Hamiltonian H_2 can be diagonalised and yields the spin-wave
 320 dispersion

$$\omega_2(\mathbf{q}) = 2S \sqrt{J_2(\mathbf{0})^2 - J_2(\mathbf{q})^2}. \tag{10}$$

321

322

323 2.3.2 Free energy in perturbation theory and quadrupolar coupling

324 The free energy in perturbation theory can be written as $F = \sum_\ell F_\ell$, where F_ℓ is of
 325 ℓ -th order in $H_1 + H_3$, and F_0 is the unperturbed free energy of the Hamiltonian H_2 .
 326 Notice that only even-order terms are non vanishing, thus $\ell = 0, 2, 4, \dots$. Given the
 327 evolution operator in imaginary time,

$$S(\beta) = T_\tau \left(e^{-\int_0^\beta d\tau (H_1(\tau) + H_3(\tau))} \right) = \sum_\ell S_\ell(\beta), \tag{11}$$

328 where $H_a(\tau)$, $a = 1, 3$, evolves with the Hamiltonian H_2 , the second order correction
 329 to the free energy is readily found to be

$$\begin{aligned}
 F_2 &= -T \langle S_2(\beta) \rangle \\
 &= -\frac{\Xi_2(T)}{J_2} \sum_n \left[J_1^2 (\mathbf{n}_{3,1,n} \cdot \mathbf{n}_{3,2,n})^2 + J_3^2 (\mathbf{n}_{3,1,n} \cdot \mathbf{n}_{3,2,n+1})^2 \right],
 \end{aligned} \tag{12}$$

330 where

$$\Xi_2(T) = J_2 S^2 \sum_{\mathbf{q}} T \sum_{\lambda} |\gamma(\mathbf{q})|^2 \frac{J_2(\mathbf{0}) - J_2(\mathbf{q})}{J_2(\mathbf{0}) + J_2(\mathbf{q})} \left(\frac{\omega_2(\mathbf{q})}{\omega_\lambda^2 + \omega_2(\mathbf{q})^2} \right)^2 > 0, \tag{13}$$

331 with $\omega_\lambda = 2\pi\lambda T$, $\lambda \in \mathbb{Z}$, bosonic Matsubara frequencies. Even without explicitly
 332 evaluating Ξ_2 , we can conclude that the free-energy gain at second order in $H_1 +$
 333 H_3 is maximised by $\mathbf{n}_{3,1,n} \cdot \mathbf{n}_{3,2,m} = \pm 1$, with $m = n, n+1$, which reduces the
 334 classical degeneracy to 4^L configurations, where L is the total number of layers in

335 the system. Such residual degeneracy is split by a fourth order correction to the free
 336 energy proportional to $J_1^2 J_3^2$ that reads

$$F_4 = -\frac{J_1^2 J_3^2}{J_2^3} \Xi_4(T) \sum_n (\mathbf{n}_{3,1,n} \cdot \mathbf{n}_{3,2,n}) \quad (14)$$

$$\left[(\mathbf{n}_{3,1,n} \cdot \mathbf{n}_{3,2,n+1}) + (\mathbf{n}_{3,1,n-1} \cdot \mathbf{n}_{3,2,n}) \right],$$

337 where

$$\Xi_4(T) = 2S^4 J_2^3 T \sum_\lambda \sum_{\mathbf{q}} |\gamma(\mathbf{q}) \gamma(\mathbf{q} + \mathbf{Q})|^2 \frac{\omega_\lambda^2}{(\omega_\lambda^2 + \omega_2(\mathbf{q})^2)^3} > 0. \quad (15)$$

338 We remark that, despite $\omega_2(\mathbf{q})$ vanishes linearly at $\mathbf{q} = \mathbf{0}, \mathbf{Q}$, both $\Xi_2(T)$ and $\Xi_4(T)$
 339 are non-singular.

340 The fourth order correction F_4 in Eq. (14) has a twofold effect: it forces $\mathbf{n}_{3,1,n} \cdot \mathbf{n}_{3,2,n}$
 341 to be the same on all layers and, in addition, stabilises a ferromagnetic inter-layer
 342 stacking. Therefore, the ground state manifold at fourth order in $H_1 + H_3$ is spanned
 343 by $\mathbf{n}_{3,1,n} = \mathbf{n}_3$ and $\mathbf{n}_{3,2,n} = \sigma \mathbf{n}_3$, where \mathbf{n}_3 is an arbitrary unit vector reflecting the
 344 spin $SU(2)$ symmetry, and $\sigma = \pm 1$ is associated with the global $C_4 \rightarrow C_2$ symmetry
 345 breaking.

346 Similarly to the single-plane $J_1 - J_2$ model [13], the above results imply that an
 347 additional term must be added to the semiclassical spin action. Specifically, if we
 348 introduce the Ising-like fields $\sigma_n(\mathbf{R}) = \mathbf{n}_{3,1,n}(\mathbf{R}) \cdot \mathbf{n}_{3,2,n}(\mathbf{R})$ and $\sigma_{n+1/2}(\mathbf{R}) =$
 349 $\mathbf{n}_{3,1,n}(\mathbf{R}) \cdot \mathbf{n}_{3,2,n+1}(\mathbf{R})$, Eqs (12) and (14) imply that, at the leading orders in J_1
 350 and J_3 , the effective action in the continuum limit includes the quadrupolar coupling
 351 term [13]
 352

$$A_Q \simeq - \sum_n \int d\mathbf{R} \left\{ \frac{\Xi_2(T)}{T J_2} \left(J_1^2 \sigma_n(\mathbf{R})^2 + J_3^2 \sigma_{n+1/2}(\mathbf{R})^2 \right) \right. \quad (16)$$

$$\left. + \frac{\Xi_4(T) J_1^2 J_3^2}{T J_2^3} \sigma_n(\mathbf{R}) \left(\sigma_{n+1/2}(\mathbf{R}) + \sigma_{n-1/2}(\mathbf{R}) \right) \right\}.$$

353 We expect a 3D Ising transition to occur at a critical temperature T_c , below which
 354 $\langle \sigma_n(\mathbf{R}) \rangle = m_1$, $\langle \sigma_{n+1/2}(\mathbf{R}) \rangle = m_3$, with $m_1 m_3 > 0$. In turn, the Ising order should
 355 bring along the 3D AFS one below a finite Néel temperature bounded from above
 356 by T_c [20]. To get a rough estimate of the latter, based on Eq. (16) we assume that,
 357 upon integrating out the spin degrees of freedom, the classical action describes an
 358 anisotropic three-dimensional ferromagnetic Ising model with exchange constants I_1
 359 on layers n , I_3 on layers $n + 1/2$, and $I_\perp < I_1, I_3$ between layers. Hereafter, we take
 360 for simplicity $J_1 = J_3$, thus $I_1 = I_3 \equiv I_\parallel$.

361 We then note that, for the $J_1 - J_2 - J_3$ model with $J_2 \simeq 9.3$ meV and
 362 $J_1 = J_3 \simeq -1.17$ meV, the 2D Ising critical temperature with $S = 3/2$ of each layer n
 363 and $n + 1/2$ is about $0.4(S + 1/2)^2 J_2 \simeq 173$ K [30]. This critical temperature corre-
 364 sponds to $I_\parallel \simeq 6.6$ meV in the 2D Ising model. The 3D Ising critical temperature T_c
 365 grows with I_\perp , reaching 280 K and 345 K at $I_\perp = 0.5 I_\parallel$ and $I_\perp = I_\parallel$, respectively [33],
 366 which are reassuringly of the same order of magnitude as T_N .

367

368 However, BaCoS₂ remains orthorhombic above T_N , which implies that the structural
 369 $C_4 \rightarrow C_2$ symmetry breaking occurs earlier than magnetic ordering upon cooling.
 370 Therefore, even though the effects of the orthorhombic distortion on the electronic
 371 structure are rather small, see Table 4, it is worth repeating the above discussion
 372 assuming from the start that $\sigma_n(\mathbf{R}) = \mathbf{n}_{3,1,n}(\mathbf{R}) \cdot \mathbf{n}_{3,2,n}(\mathbf{R}) = 1$ (AFS-a), so that
 373 $\sigma_{n+1/2}(\mathbf{R}) = \mathbf{n}_{3,1,n}(\mathbf{R}) \cdot \mathbf{n}_{3,2,n+1}(\mathbf{R}) = \mathbf{n}_{3,1,n}(\mathbf{R}) \cdot \mathbf{n}_{3,1,n+1}(\mathbf{R})$. It follows that the
 374 quadrupolar term (16) becomes

$$A_Q \simeq - \sum_n \int d\mathbf{R} \left\{ K(T) \left(\mathbf{n}_{3,1,n}(\mathbf{R}) \cdot \mathbf{n}_{3,1,n+1}(\mathbf{R}) \right)^2 \right. \\ \left. + h(T) \mathbf{n}_{3,1,n}(\mathbf{R}) \cdot \mathbf{n}_{3,1,n+1}(\mathbf{R}) \right\}, \quad (17)$$

375 with $K(T) \gg h(T) > 0$. The term proportional to $K(T)$ is bi-quadratic in the origi-
 376 nal spin operators and, alone, it would drive an Ising-like transition either towards
 377 C-AFS, $\mathbf{n}_{3,1,n} \cdot \mathbf{n}_{3,1,n+1} = 1$ or G-AFS, $\mathbf{n}_{3,1,n} \cdot \mathbf{n}_{3,1,n+1} = -1$. On the contrary, the
 378 term proportional to $h(T)$ is quadratic and yields an inter-layer ferromagnetic coupling
 379 that stabilises C-AFS, though by only two kelvins according to our DFT+U calcula-
 380 tions. Therefore, (17) corresponds to an unusual model of coupled Heisenberg layers
 381 in which the dominant inter-layer coupling is bi-quadratic. We believe that this term
 382 is responsible of the higher T_N than the estimate obtained assuming just the small
 383 ferromagnetic exchange, as earlier discussed, as well as of the pronounced Ising-like
 384 character of the Néel transition. We also remark that which among C-AFS and G-AFS
 385 is lower in energy does depend on the orbital configurations, see Table 3. Therefore,
 386 we expect that the neglected coupling between spins and orbital fluctuations should
 387 further reduce the already small energy difference between C-AFS and G-AFS.

388 3 Conclusion

389 BaCoS₂ is a frustrated magnet with a pronounced two-dimensional character of the
 390 magnetic excitations that, nonetheless, orders magnetically at a Néel temperature of
 391 $T_N \sim 300$ K [18, 19] through a second order phase transition more similar to an
 392 Ising than a Heisenberg one. We have shown that these puzzling features can be
 393 pieced together within an order-from-disorder scenario that we have uncovered by a
 394 thorough *ab initio* analysis demonstrating the critical role of the specific Co *d*-orbitals
 395 involved in magnetism. Although specific to BaCoS₂, our results might be relevant
 396 to other spin-frustrated transition metal compounds that also crystallise in the non-
 397 symmorphic $P4/nmm$ space group, like, e.g., the iron pnictides. In many (mainly
 398 electron-doped) iron-based superconductors the disordered phase at high temperature
 399 first spontaneously breaks C_4 symmetry when cooling below a critical temperature
 400 T_{nem} , thus entering a nematic phase [34]. Only at a lower temperature $T_N < T_{\text{nem}}$, also
 401 spin $SU(2)$ is broken and a stripe-ordered magnetic long-range order emerges [34, 35].
 402 The Néel temperature can be quite large as in BaCoS₂ or even vanishing within
 403 experimental accuracy as in FeSe, where $T_N \neq 0$ is observed only under pressure [36].
 404 Also from a model point of view, our description of BaCoS₂ fits into the modelling of

405 these materials. Indeed, the key role played by several order parameters in BaCoS₂
406 has parallels to the phenomenological Landau free energy description of FeSC [34].
407 Besides itinerant multi-orbital Hubbard models [37–39], also spin-1 Heisenberg models
408 conceptually similar to ours have been proposed for iron-based superconductors and
409 FeSe [40, 41]. There, however, instead of achieving the C_4 symmetry breaking via an
410 order-from-disorder phenomenon, it is often assumed from the start [42] or by explicitly
411 adding bi-quadratic spin exchanges [40] that mimic the quadrupolar terms (16).
412 Moreover, our *ab initio* simulations for BaCoS₂ predict that the lowest-energy phase
413 has not ferro-orbital order, as often discussed in the context of FeSC, but rather
414 an anti-ferro orbital ordering that breaks the non-symmorphic symmetry instead of
415 C_4 . Therefore, BaCoS₂ seems to realise a situation where collinear magnetism and
416 orthorhombicity do not imply orbital nematicity, unless for specific crystal structures
417 under pressure.

418 4 Methods

419 Ab initio calculations

420 We carried out *ab initio* DFT and DFT+U calculations using the Quantum
421 ESPRESSO package [43, 44]. The density functional is of generalized gradient approx-
422 imation type, namely the Perdew-Burke-Ernzerhof functional [45], on which local
423 Hubbard interactions and Hund’s coupling terms were added to the Co atoms in case
424 of the DFT+U within a fully rotational invariant framework [46, 47]. If not stated
425 otherwise, the geometry of the unit cell and the internal coordinates of the atomic
426 positions in the orthorhombic structure were those determined experimentally, taken
427 from Ref. [25]. For non-magnetic calculations, the relative atomic positions were kept
428 fixed and the in-plane lattice constants $a = b$ chosen such that the unit cell volume
429 matched the one of the orthorhombic structure. Co and S atoms are described by
430 norm-conserving pseudopotentials (PP) with non-linear core corrections, Ba atoms
431 are described by ultrasoft pseudopotentials. The Co PP contains 13 valence electrons
432 ($3s^2, 3p^6, 3d^7$), the Ba PP 10 electrons ($5s^2, 5p^6, 6s^2$), and S PPs are in a ($3s^2, 3p^3$)
433 configuration. The plane-waves cutoff has been set to 120Ry and we used a Gaussian
434 smearing of 0.01Ry. The k -point sampling of the electron-momentum grid was at
435 least $8 \times 8 \times 8$ points in the 8 Co atom supercell.

437 Wannier interpolation

438 To determine the band structure and derive an effective low-energy model, we per-
439 formed a Wannier interpolation with maximally localised Wannier functions [48, 49]
440 using the Wannier90 package [50]. We constructed Wannier fits based on the non-
441 magnetic DFT+U calculation using a $4 \times 4 \times 4$ k-grid with a doubled in-plane unit
442 cell comprising 4 Co atoms.

443 **Acknowledgments.** We are thankful to H. Abushammala, A. Gauzzi, and Y. Klein
444 for fruitful discussions. We acknowledge the allocation for computer resources by the
445 French Grand Équipement National de Calcul Intensif (GENCI) under the project

446 numbers A0110906493 and A0110912043. M.F. acknowledges financial support from
447 the European Research Council (ERC), under the European Union’s Horizon 2020
448 research and innovation programme, Grant agreement No. 692670 ”FIRSTORM”.

449 **Declarations**

450 **Data availability**

451 The data used for generating the figures of the main text and the Supplementary
452 Information are available from the corresponding author on reasonable request.

453 **Competing interests**

454 The authors declare no competing interests.

455 **Code availability**

456 The codes used and described in the Methods section are publicly available. The
457 scripts used for generating the figures are available from the corresponding author on
458 reasonable request.

459 **Contributions**

460 M.C. and B.L. designed the research, B.L. performed the DFT+U calculations and
461 M.F. developed the model. All authors analysed the data, discussed the results and
462 wrote the manuscript.

463 **Corresponding author**

464 Correspondence to Benjamin Lenz.

465 **References**

- 466 [1] Rau, J.G., McClarty, P.A., Moessner, R.: Pseudo-Goldstone Gaps and Order-by-
467 Quantum Disorder in Frustrated Magnets. *Phys. Rev. Lett.* **121**, 237201 (2018)
468 <https://doi.org/10.1103/PhysRevLett.121.237201>
- 469 [2] Schick, R., Ziman, T., Zhitomirsky, M.E.: Quantum versus thermal fluctuations
470 in the fcc antiferromagnet: Alternative routes to order by disorder. *Phys. Rev. B*
471 **102**, 220405 (2020) <https://doi.org/10.1103/PhysRevB.102.220405>
- 472 [3] Villain, J., Bidaux, R., Carton, J.P., Conte, R.: Order as an effect of disorder. *J. Phys. France* **41**(11), 1263–1272 (1980) [https://doi.org/10.1051/jphys:
473 0198000410110126300](https://doi.org/10.1051/jphys:0198000410110126300)
- 474
475 [4] Burgess, C.: Goldstone and pseudo-Goldstone bosons in nuclear, particle and
476 condensed-matter physics. *Physics Reports* **330**(4), 193–261 (2000) [https://doi.
477 org/10.1016/s0370-1573\(99\)00111-8](https://doi.org/10.1016/s0370-1573(99)00111-8)

- 478 [5] Weinberg, S.: Approximate Symmetries and Pseudo-Goldstone Bosons. Phys.
479 Rev. Lett. **29**, 1698–1701 (1972) <https://doi.org/10.1103/PhysRevLett.29.1698>
- 480 [6] Coleman, S., Weinberg, E.: Radiative Corrections as the Origin of Spontaneous
481 Symmetry Breaking. Phys. Rev. D **7**, 1888–1910 (1973) [https://doi.org/10.1103/](https://doi.org/10.1103/PhysRevD.7.1888)
482 [PhysRevD.7.1888](https://doi.org/10.1103/PhysRevD.7.1888)
- 483 [7] Demler, E., Hanke, W., Zhang, S.-C.: $SO(5)$ theory of antiferromagnetism and
484 superconductivity. Rev. Mod. Phys. **76**, 909–974 (2004) [https://doi.org/10.1103/](https://doi.org/10.1103/RevModPhys.76.909)
485 [RevModPhys.76.909](https://doi.org/10.1103/RevModPhys.76.909)
- 486 [8] Fernandes, R.M., Chubukov, A.V.: Low-energy microscopic models for iron-based
487 superconductors: a review. Reports on Progress in Physics **80**(1), 014503 (2016)
488 <https://doi.org/10.1088/1361-6633/80/1/014503>
- 489 [9] Tessman, J.R.: Magnetic Anisotropy at 0°K. Phys. Rev. **96**, 1192–1195 (1954)
490 <https://doi.org/10.1103/PhysRev.96.1192>
- 491 [10] Belorizky, E., Casalegno, R., Niez, J.J.: Calculation of the Spin Wave Energy Gap
492 at $k = 0$ for a Simple Cubic Ferromagnet with Anisotropic Exchange Interactions.
493 physica status solidi (b) **102**(1), 365–372 (1980) [https://doi.org/10.1002/pssb.](https://doi.org/10.1002/pssb.2221020135)
494 [2221020135](https://doi.org/10.1002/pssb.2221020135) <https://onlinelibrary.wiley.com/doi/pdf/10.1002/pssb.2221020135>
- 495 [11] Shender, E.: Anti-ferromagnetic garnets with fluctuation-like interacting sub-
496 lattices. Zh. Éksp. Teor. Fiz. **83**(1), 326–337 (1982). [Sov. Phys. JETP **56**, 178
497 (1982)]
- 498 [12] Henley, C.L.: Ordering due to disorder in a frustrated vector antiferromagnet.
499 Phys. Rev. Lett. **62**, 2056–2059 (1989) [https://doi.org/10.1103/PhysRevLett.62.](https://doi.org/10.1103/PhysRevLett.62.2056)
500 [2056](https://doi.org/10.1103/PhysRevLett.62.2056)
- 501 [13] Chandra, P., Coleman, P., Larkin, A.I.: Ising transition in frustrated heisenberg
502 models. Phys. Rev. Lett. **64**, 88–91 (1990) [https://doi.org/10.1103/PhysRevLett.](https://doi.org/10.1103/PhysRevLett.64.88)
503 [64.88](https://doi.org/10.1103/PhysRevLett.64.88)
- 504 [14] Gvozdkova, M.V., Zhitomirsky, M.E.: A Monte Carlo study of the first-order
505 transition in a Heisenberg FCC antiferromagnet. Journal of Experimental and
506 Theoretical Physics Letters **81**(5), 236–240 (2005) [https://doi.org/10.1134/1.](https://doi.org/10.1134/1.1921323)
507 [1921323](https://doi.org/10.1134/1.1921323)
- 508 [15] Rau, J.G., Lee, E.K.-H., Kee, H.-Y.: Generic Spin Model for the Honeycomb
509 Iridates beyond the Kitaev Limit. Phys. Rev. Lett. **112**, 077204 (2014) <https://doi.org/10.1103/PhysRevLett.112.077204>
510 <https://doi.org/10.1103/PhysRevLett.112.077204>
- 511 [16] Shamoto, S.-i., Kodama, K., Harashina, H., Sato, M., Kakurai, K.: Neu-
512 tron Scattering Study of $BaCo_{0.82}Ni_{0.18}S_2$. Journal of the Physical Soci-
513 ety of Japan **66**(4), 1138–1144 (1997) <https://doi.org/10.1143/JPSJ.66.1138>

- 514 <https://journals.jps.jp/doi/pdf/10.1143/JPSJ.66.1138>
- 515 [17] Shamoto, S.-i., Yamauchi, H., Ikeuchi, K., Kajimoto, R., Ieda, J.: Broken C_4
516 symmetry in the tetragonal state of uniaxial strained $\text{BaCo}_{0.9}\text{Ni}_{0.1}\text{S}_{1.9}$. *Phys. Rev.*
517 *Research* **3**, 013169 (2021) <https://doi.org/10.1103/PhysRevResearch.3.013169>
- 518 [18] Abushammala, H., Lenz, B., Baptiste, B., Santos-Cottin, D., Toulemonde,
519 P., Casula, M., Klein, Y., Gauzzi, A.: Two-dimensional fluctuations and
520 competing phases in the stripe-like antiferromagnet BaCoS_2 . *arXiv e-prints*,
521 2302–12208 (2023) <https://doi.org/10.48550/arXiv.2302.12208> [arXiv:2302.12208](https://arxiv.org/abs/2302.12208)
522 [cond-mat.str-el]
- 523 [19] Mandrus, D., Sarrao, J.L., Chakoumakos, B.C., Fernandez-Baca, J.A., Nagler,
524 S.E., Sales, B.C.: Magnetism in BaCoS_2 . *Journal of Applied Physics* **81**(8), 4620–
525 4622 (1997) <https://doi.org/10.1063/1.365182> <https://doi.org/10.1063/1.365182>
- 526 [20] Syljuåsen, O.F., Paaske, J., Schechter, M.: Interplay between magnetic and vestigi-
527 al nematic orders in the layered $J_1 - J_2$ classical Heisenberg model. *Phys. Rev.*
528 *B* **99**, 174404 (2019) <https://doi.org/10.1103/PhysRevB.99.174404>
- 529 [21] Juhász Junger, I., Ihle, D., Richter, J.: Thermodynamics of layered Heisenberg
530 magnets with arbitrary spin. *Phys. Rev. B* **80**, 064425 (2009) [https://doi.org/10.](https://doi.org/10.1103/PhysRevB.80.064425)
531 [1103/PhysRevB.80.064425](https://doi.org/10.1103/PhysRevB.80.064425)
- 532 [22] Santos-Cottin, D., Casula, M., Lantz, G., Klein, Y., Petaccia, L., Le Fèvre, P.,
533 Bertran, F., Papalazarou, E., Marsi, M., Gauzzi, A.: Rashba coupling amplifi-
534 cation by a staggered crystal field. *Nature Communications* **7**(1), 11258 (2016)
535 <https://doi.org/10.1038/ncomms11258>
- 536 [23] Brosco, V., Capone, M.: Rashba-metal to Mott-insulator transition. *Phys. Rev.*
537 *B* **101**, 235149 (2020) <https://doi.org/10.1103/PhysRevB.101.235149>
- 538 [24] Santos-Cottin, D., Klein, Y., Werner, P., Miyake, T., Medici, L., Gauzzi, A., Lobo,
539 R.P.S.M., Casula, M.: Linear behavior of the optical conductivity and incoherent
540 charge transport in BaCoS_2 . *Phys. Rev. Materials* **2**, 105001 (2018) [https://doi.](https://doi.org/10.1103/PhysRevMaterials.2.105001)
541 [org/10.1103/PhysRevMaterials.2.105001](https://doi.org/10.1103/PhysRevMaterials.2.105001)
- 542 [25] Snyder, G.J., Gelabert, M.C., DiSalvo, F.J.: Refined Structure and Properties of
543 the Layered Mott Insulator BaCoS_2 . *Journal of Solid State Chemistry* **113**(2),
544 355–361 (1994) <https://doi.org/10.1006/jssc.1994.1380>
- 545 [26] Kodama, K., Shamoto, S.-i., Harashina, H., Takeda, J., Sato, M., Kakurai, K.,
546 Nishi, M.: Electronic Structure of the Quasi Two-Dimensional Mott System
547 $\text{BaCo}_{1-x}\text{Ni}_x\text{S}_2$. *Journal of the Physical Society of Japan* **65**(6), 1782–1786 (1996)
548 <https://doi.org/10.1143/JPSJ.65.1782> <https://doi.org/10.1143/JPSJ.65.1782>
- 549 [27] Schueller, E.C., Miller, K.D., Zhang, W., Zuo, J.L., Rondinelli, J.M., Wilson,

- 550 S.D., Seshadri, R.: Structural signatures of the insulator-to-metal transition in
551 $\text{BaCo}_{1-x}\text{Ni}_x\text{S}_2$. *Phys. Rev. Materials* **4**, 104401 (2020) [https://doi.org/10.1103/](https://doi.org/10.1103/PhysRevMaterials.4.104401)
552 [PhysRevMaterials.4.104401](https://doi.org/10.1103/PhysRevMaterials.4.104401)
- 553 [28] Zainullina, V.M., Korotin, M.A.: Ground state of BaCoS_2 as a set of energy-
554 degenerate orbital-ordered configurations of Co^{2+} ions. *Physics of the Solid State*
555 **53**(5), 978–984 (2011)
- 556 [29] Moreo, A., Dagotto, E., Jolicoeur, T., Riera, J.: Incommensurate correlations in
557 the t-J and frustrated spin-1/2 Heisenberg models. *Phys. Rev. B* **42**, 6283–6293
558 (1990) <https://doi.org/10.1103/PhysRevB.42.6283>
- 559 [30] Capriotti, L., Fubini, A., Roscilde, T., Tognetti, V.: Ising Transition in the Two-
560 Dimensional Quantum $J_1 - J_2$ Heisenberg Model. *Phys. Rev. Lett.* **92**, 157202
561 (2004) <https://doi.org/10.1103/PhysRevLett.92.157202>
- 562 [31] Weber, C., Becca, F., Mila, F.: Finite-temperature properties of frustrated classi-
563 cal spins coupled to the lattice. *Phys. Rev. B* **72**, 024449 (2005) [https://doi.org/](https://doi.org/10.1103/PhysRevB.72.024449)
564 [10.1103/PhysRevB.72.024449](https://doi.org/10.1103/PhysRevB.72.024449)
- 565 [32] Lante, V., Parola, A.: Ising phase in the $J_1 - J_2$ Heisenberg model. *Phys. Rev. B*
566 **73**, 094427 (2006) <https://doi.org/10.1103/PhysRevB.73.094427>
- 567 [33] Oitmaa, J., Enting, I.G.: Critical behaviour of the anisotropic Ising model. *Jour-
568 nal of Physics C: Solid State Physics* **5**(2), 231 (1972) [https://doi.org/10.1088/](https://doi.org/10.1088/0022-3719/5/2/012)
569 [0022-3719/5/2/012](https://doi.org/10.1088/0022-3719/5/2/012)
- 570 [34] Fernandes, R.M., Chubukov, A.V., Schmalian, J.: What drives nematic order in
571 iron-based superconductors? *Nature Physics* **10**(2), 97–104 (2014) [https://doi.](https://doi.org/10.1038/nphys2877)
572 [org/10.1038/nphys2877](https://doi.org/10.1038/nphys2877)
- 573 [35] Wang, F., Kivelson, S.A., Lee, D.-H.: Nematicity and quantum paramagnetism in
574 FeSe . *Nature Physics* **11**(11), 959–963 (2015) <https://doi.org/10.1038/nphys3456>
- 575 [36] Kothapalli, K., Böhmer, A.E., Jayasekara, W.T., Ueland, B.G., Das, P., Sapkota,
576 A., Taufour, V., Xiao, Y., Alp, E., Bud’ko, S.L., Canfield, P.C., Kreyssig, A.,
577 Goldman, A.I.: Strong cooperative coupling of pressure-induced magnetic order
578 and nematicity in FeSe . *Nature Communications* **7**(1), 12728 (2016) [https://doi.](https://doi.org/10.1038/ncomms12728)
579 [org/10.1038/ncomms12728](https://doi.org/10.1038/ncomms12728)
- 580 [37] Chubukov, A.V., Efremov, D.V., Eremin, I.: Magnetism, superconductivity, and
581 pairing symmetry in iron-based superconductors. *Phys. Rev. B* **78**, 134512 (2008)
582 <https://doi.org/10.1103/PhysRevB.78.134512>
- 583 [38] Stanev, V., Kang, J., Tesanovic, Z.: Spin fluctuation dynamics and multiband
584 superconductivity in iron pnictides. *Phys. Rev. B* **78**, 184509 (2008) [https://doi.](https://doi.org/10.1103/PhysRevB.78.184509)
585 [org/10.1103/PhysRevB.78.184509](https://doi.org/10.1103/PhysRevB.78.184509)

- 586 [39] Graser, S., Maier, T.A., Hirschfeld, P.J., Scalapino, D.J.: Near-degeneracy of sev-
587 eral pairing channels in multiorbital models for the Fe pnictides. *New Journal of*
588 *Physics* **11**(2), 025016 (2009) <https://doi.org/10.1088/1367-2630/11/2/025016>
- 589 [40] Hu, J., Xu, B., Liu, W., Hao, N.-N., Wang, Y.: Unified minimum effective model
590 of magnetic properties of iron-based superconductors. *Phys. Rev. B* **85**, 144403
591 (2012) <https://doi.org/10.1103/PhysRevB.85.144403>
- 592 [41] Glasbrenner, J.K., Mazin, I.I., Jeschke, H.O., Hirschfeld, P.J., Fernandes, R.M.,
593 Valentí, R.: Effect of magnetic frustration on nematicity and superconductivity
594 in iron chalcogenides. *Nature Physics* **11**(11), 953–958 (2015) [https://doi.org/10.](https://doi.org/10.1038/nphys3434)
595 [1038/nphys3434](https://doi.org/10.1038/nphys3434)
- 596 [42] Zhao, J., Adroja, D.T., Yao, D.-X., Bewley, R., Li, S., Wang, X.F., Wu, G., Chen,
597 X.H., Hu, J., Dai, P.: Spin waves and magnetic exchange interactions in CaFe_2As_2 .
598 *Nature Physics* **5**(8), 555–560 (2009) <https://doi.org/10.1038/nphys1336>
- 599 [43] Giannozzi, P., Baroni, S., Bonini, N., Calandra, M., Car, R., Cavazzoni, C.,
600 Ceresoli, D., Chiarotti, G.L., Cococcioni, M., Dabo, I., Corso, A.D., Giron-
601 coli, S., Fabris, S., Fratesi, G., Gebauer, R., Gerstmann, U., Gougoussis, C.,
602 Kokalj, A., Lazzeri, M., Martin-Samos, L., Marzari, N., Mauri, F., Mazzarello, R.,
603 Paolini, S., Pasquarello, A., Paulatto, L., Sbraccia, C., Scandolo, S., Sclauzero,
604 G., Seitsonen, A.P., Smogunov, A., Umari, P., Wentzcovitch, R.M.: QUANTUM
605 ESPRESSO: a modular and open-source software project for quantum simula-
606 tions of materials. *Journal of Physics: Condensed Matter* **21**(39), 395502 (2009)
607 <https://doi.org/10.1088/0953-8984/21/39/395502>
- 608 [44] Giannozzi, P., Andreussi, O., Brumme, T., Bunau, O., Nardelli, M.B., Calandra,
609 M., Car, R., Cavazzoni, C., Ceresoli, D., Cococcioni, M., Colonna, N., Carnimeo,
610 I., Corso, A.D., Gironcoli, S., Delugas, P., DiStasio, R.A., Ferretti, A., Floris,
611 A., Fratesi, G., Fugallo, G., Gebauer, R., Gerstmann, U., Giustino, F., Gorni,
612 T., Jia, J., Kawamura, M., Ko, H.-Y., Kokalj, A., Küçükbenli, E., Lazzeri, M.,
613 Marsili, M., Marzari, N., Mauri, F., Nguyen, N.L., Nguyen, H.-V., Otero-de-la-
614 Roza, A., Paulatto, L., Poncé, S., Rocca, D., Sabatini, R., Santra, B., Schlipf, M.,
615 Seitsonen, A.P., Smogunov, A., Timrov, I., Thonhauser, T., Umari, P., Vast, N.,
616 Wu, X., Baroni, S.: Advanced capabilities for materials modelling with Quantum
617 ESPRESSO. *Journal of Physics: Condensed Matter* **29**(46), 465901 (2017) <https://doi.org/10.1088/1361-648x/aa8f79>
618
- 619 [45] Perdew, J.P., Burke, K., Ernzerhof, M.: Generalized Gradient Approximation
620 Made Simple. *Phys. Rev. Lett.* **77**, 3865–3868 (1996) [https://doi.org/10.1103/](https://doi.org/10.1103/PhysRevLett.77.3865)
621 [PhysRevLett.77.3865](https://doi.org/10.1103/PhysRevLett.77.3865)
- 622 [46] Anisimov, V.I., Zaanen, J., Andersen, O.K.: Band theory and Mott insulators:
623 Hubbard U instead of Stoner I. *Phys. Rev. B* **44**, 943–954 (1991) [https://doi.org/](https://doi.org/10.1103/PhysRevB.44.943)
624 [10.1103/PhysRevB.44.943](https://doi.org/10.1103/PhysRevB.44.943)

- 625 [47] Liechtenstein, A.I., Anisimov, V.I., Zaanen, J.: Density-functional theory and
626 strong interactions: Orbital ordering in Mott-Hubbard insulators. *Phys. Rev. B*
627 **52**, 5467–5470 (1995) <https://doi.org/10.1103/PhysRevB.52.R5467>
- 628 [48] Marzari, N., Vanderbilt, D.: Maximally localized generalized Wannier functions
629 for composite energy bands. *Phys. Rev. B* **56**, 12847–12865 (1997) <https://doi.org/10.1103/PhysRevB.56.12847>
630
- 631 [49] Souza, I., Marzari, N., Vanderbilt, D.: Maximally localized Wannier functions
632 for entangled energy bands. *Phys. Rev. B* **65**, 035109 (2001) <https://doi.org/10.1103/PhysRevB.65.035109>
633
- 634 [50] Mostofi, A.A., Yates, J.R., Pizzi, G., Lee, Y.-S., Souza, I., Vanderbilt, D., Marzari,
635 N.: An updated version of wannier90: A tool for obtaining maximally-localised
636 Wannier functions. *Computer Physics Communications* **185**(8), 2309–2310 (2014)
637 <https://doi.org/10.1016/j.cpc.2014.05.003>
- 638 [51] Kanada, M., Harashina, H., Sasaki, H., Kodama, K., Sato, M., Kakurai, K., Nishi,
639 M., Nishibori, E., Sakata, M., Takata, M., Adachi, T.: High-pressure neutron and
640 X-ray studies on the Mott transition of BaCoS₂. *Journal of Physics and Chem-*
641 *istry of Solids* **60**(8), 1181–1183 (1999) [https://doi.org/10.1016/S0022-3697\(99\)](https://doi.org/10.1016/S0022-3697(99)00078-5)
642 [00078-5](https://doi.org/10.1016/S0022-3697(99)00078-5)

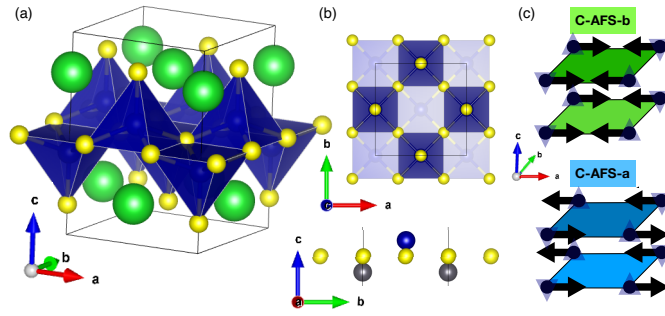


Fig. 1 Crystal structure of BaCoS_2 . (a) Three-dimensional view of tetragonal BaCoS_2 . Ba atoms are the large green spheres, while S atoms are shown in yellow. The cobalt atoms sit inside the blue square-based pyramids. (b) Top and lateral view of the structure, respectively. Note that, since the apexes of nearest neighbour pyramids point in opposite directions, there are two inequivalent Co atoms, shown as blue and grey spheres, with opposite vertical displacements from the $a - b$ plane, which are connected by the non-symmorphic symmetry. (c) Magnetic order in the low-temperature orthorhombic phase. Dots represent Co atoms, arrows their spins and blue triangles indicate the orientation of the surrounding sulfur pyramids. Within each $a - b$ plane the spins form a striped antiferromagnet (AFS) with ferromagnetic chains coupled antiferromagnetically. The ferromagnetic chains can be either along a (AFS-a) or along b (AFS-b). The planes are stacked ferromagnetically, C-type stacking, thus the two equivalent configurations C-AFS-a and C-AFS-b.

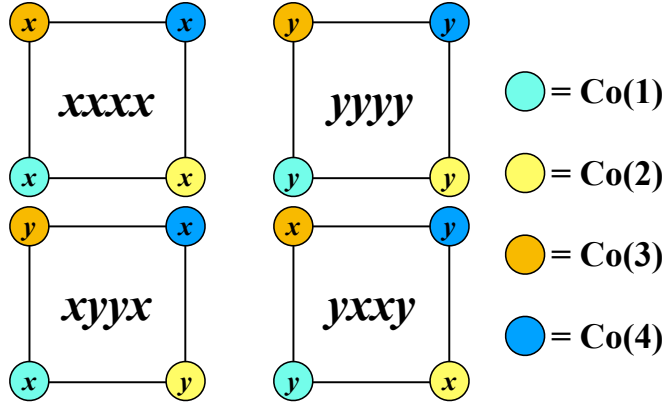


Fig. 2 Illustration of the orbital arrangements within BaCoS_2 allowed by the $Cmme$ space group. Co(1), Co(2), Co(3) and Co(4) correspond to the $4g$ Wyckoff positions occupied by the cobalt atoms. The label $x(y)$ indicates that the hole occupies the $d_{xz}(d_{yz})$ orbital of the $3/4$ -filled d_{xz}/d_{yz} doublet of the corresponding cobalt atom.

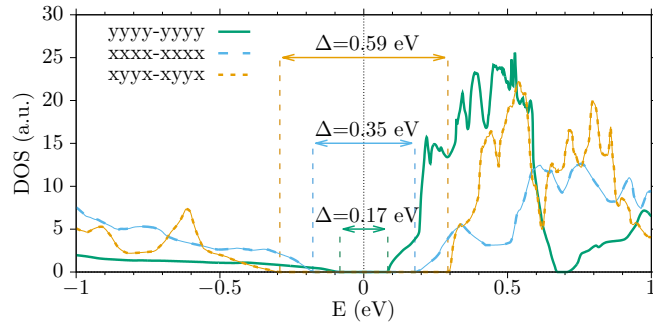


Fig. 3 Density of states for different orbital configurations. The density of states (DOS) around the Fermi level is shown for the two orbital nematic configurations $yyyy$ (full green line) and $xxxx$ (dashed blue line) as well as for the orbital ordered configuration $xyyx$ (dashed orange line), which is found to be lowest in energy within Hubbard- U corrected density functional theory (DFT+ U) calculations.

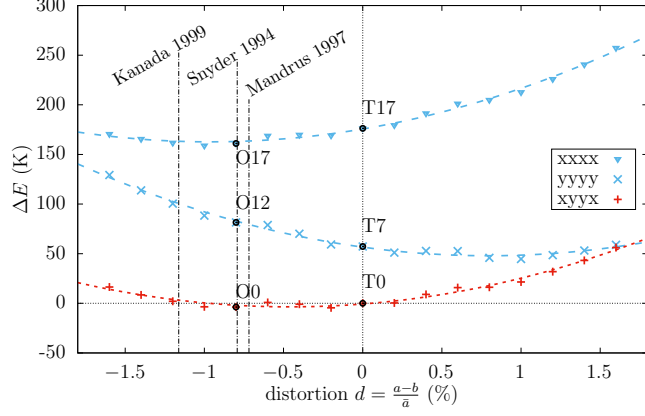


Fig. 4 Phase stability upon orthorhombic distortions. Energy ΔE per formula unit as function of the orthorhombic distortion d at fixed unit cell volume and measured with respect to the $C(xyyx)$ phase at $d = 0$ (T0 in Table 1). We compare $C(xyyx)$ with the two nematic configurations $C(xxxx)$ and $C(yyyy)$ assuming a magnetic order C-AFS-a. Experimental data are taken from Refs. [19, 25, 51]. The phases T0, T7, and T17 refer to Table 1, phases O0, O12, and O17 to Table 3.

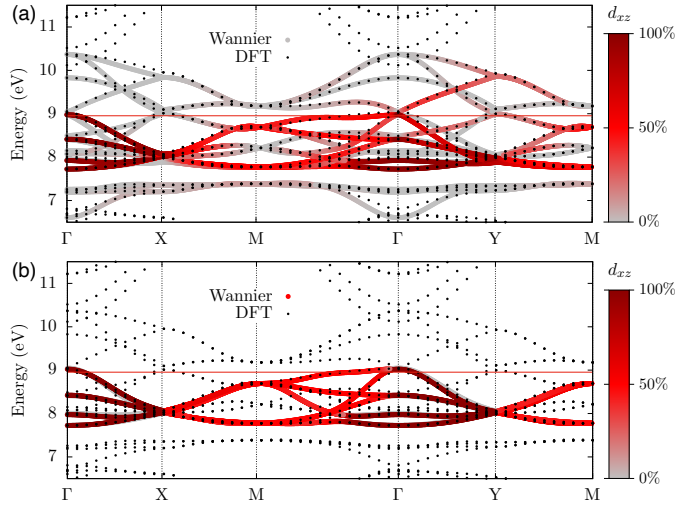


Fig. 5 Wannierization of the density functional theory (DFT) band structure. DFT band structure and eigenstates of our Wannier Hamiltonians along the high-symmetry path $\Gamma - X - M - \Gamma - Y - M$: (a) Co- d model and (b) d_{xz} - d_{yz} model with projection onto the d_{xz} -orbital character in red.

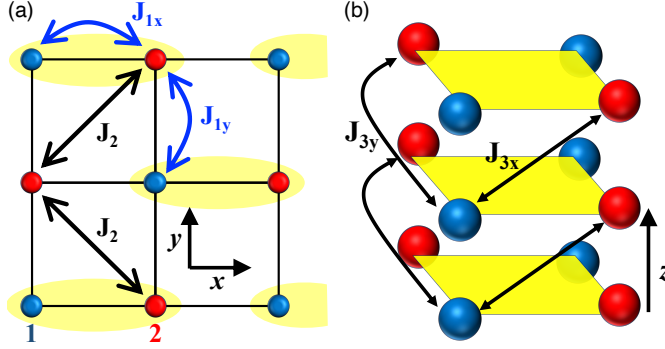


Fig. 6 Effective Heisenberg spin model for BaCoS_2 . Panel (a) shows the $J_1 - J_2$ model on the $a - b$ plane, while panel (b) shows how nearest neighbour planes are coupled to each other by the exchange J_3 . The latter forces to deal with a two-site unit cell, highlighted in yellow in panel (a). Blue and red balls indicate the two different Co sites of the unit cell.

spin and orbital configurations	$E(\text{Kelvin})$	#
C-AFS-a-C($xyyx$)	0	T0
G-AFS-a-C($xyyx$)	2	T1
C-AFS-a-G($xyyx$)	14	T2
G-AFS-a-G($xyyx$)	22	T3
G-AFS-a-G($xyxy$)	50	T4
C-AFS-a-G($xyxy$)	52	T5
C-AFS-a-C($xyxy$)	52	T6
C-AFS-a-C($yyyy$)	57	T7
G-AFS-a-C($xyxy$)	64	T8
G-AFS-a-C($yyyy$)	73	T9
C-AFS-a-G($xyyy$)	79	T10
C-AFS-a-G($yyyy$)	86	T11
G-AFS-a-G($yyyy$)	89	T12
G-AFS-a-C($xyyy$)	89	T13
C-AFS-a-C($xyyy$)	93	T14
G-AFS-a-G($xyyy$)	95	T15
G-AFS-a-C($xxxx$)	171	T16
C-AFS-a-C($xxxx$)	176	T17

Table 1 *Ab initio* energies of the tetragonal phase. Hubbard- U corrected density functional theory (DFT+ U) energies ($U = 2.8$ eV) in Kelvin and per formula unit of the low-lying spin and orbital configurations in the tetragonal structure with an 8-site unit cell, assuming an antiferromagnetic stripe order along a (AFS- a), being degenerate with AFS- b . The lowest energy state sets the zero of energy. Note that some states are doubly degenerate, for instance $C(xyxx)$ is degenerate with $C(yxyx)$ as well as $G(yyyy)$ is degenerate with $G(xxxx)$, and thus we just indicate one of them. Moreover, the table includes also configurations not allowed by the $Cmme$ orthorhombic space group, which, nonetheless, represent alternative symmetry-breaking paths from the tetragonal structure. Each state is labelled by Tn , T referring to the tetragonal phase and n being the ascending order in energy.

(a)

orbital configuration	E	ΔE
$yyyx$	$-2\Gamma_1$	0
$xyxy$	$-2\sigma\delta\Gamma_1$	$2\Gamma_1 - 2\sigma\delta\Gamma_1$
$xyxy$	$2\sigma\delta\Gamma_1$	$2\Gamma_1 + 2\sigma\delta\Gamma_1$
$xxxx$	$2\Gamma_1 - \sigma B_\tau$	$4\Gamma_1 - \sigma B_\tau$
$yyyy$	$2\Gamma_1 + \sigma B_\tau$	$4\Gamma_1 + \sigma B_\tau$

(b)

	Γ_1 (K)	$\delta\Gamma_1$ (K)	B_τ (K)
C-AFS	33 ± 4	10	60
G-AFS	31 ± 4	6	49

Table 2 Ising model for the

tetragonal phase. The energies of the different orbital configurations within an assumed nearest neighbour antiferromagnetic Ising model with exchange constants $\Gamma_1 + \sigma\delta\Gamma_1$ along a , $\Gamma_1 - \sigma\delta\Gamma_1$ along b , and uniform pseudo-magnetic field σB_τ are listed in (a). The values of those parameters extracted through Table 1 for antiferromagnetic stripe (AFS) ordering are shown in (b). We just consider the C-type orbital stacked configurations, since the G-type ones do not allow fixing B_τ .

spin and orbital configurations	$E(\text{Kelvin})$	#
C-AFS-a-C($xyyx$)	0	O0
G-AFS-a-C($xyyx$)	2	O1
C-AFS-a-G($xyyx$)	14	O2
C-AFS-b-C($xyyx$)	20	O3
G-AFS-a-G($xyyx$)	22	O4
G-AFS-b-C($xyyx$)	22	O5
C-AFS-b-G($xyyx$)	34	O6
G-AFS-b-G($xyyx$)	42	O7
C-AFS-b-C($xxxx$)	50	O8
G-AFS-b-C($xxxx$)	65	O9
C-AFS-b-G($xxxx$)	79	O10
G-AFS-b-G($xxxx$)	82	O11
C-AFS-a-C($yyyy$)	85	O12
C-AFS-a-G($xxxx$)	93	O13
G-AFS-a-G($xxxx$)	96	O14
G-AFS-a-C($yyyy$)	101	O15
G-AFS-a-C($xxxx$)	160	O16
C-AFS-a-C($xxxx$)	165	O17
G-AFS-b-C($yyyy$)	203	O18
C-AFS-b-C($yyyy$)	209	O19

Table 3 Ab initio energies of the orthorhombic phase. Same as in Table 1 but for the orthorhombic structure with $b > a$, $b/a = 1.008$. In this case, antiferromagnetic stripe order along a (AFS-a) and AFS-b are not degenerate, and thus both have been studied. Only the orbital configurations allowed by symmetry are shown. The states are labelled by On , where O refers to the orthorhombic phase and n is the order.

bond direction	hopping matrix (meV)
$T_{(1,1,0)} = T_{(-1,-1,0)}$	$\begin{pmatrix} 96 & 102 \\ 102 & 94 \end{pmatrix}$
$T_{(1,-1,0)} = T_{(-1,1,0)}$	$\begin{pmatrix} 96 & -102 \\ -102 & 94 \end{pmatrix}$
$T_{(1,0,0)} = T_{(-1,0,0)}$	$\begin{pmatrix} 2 & 0 \\ 0 & -43 \end{pmatrix}$
$T_{(0,1,0)} = T_{(0,-1,0)}$	$\begin{pmatrix} -48 & 0 \\ 0 & 2 \end{pmatrix}$
$T_{(1,0,1)} = T_{(-1,0,1)}$	$\begin{pmatrix} -68 & 0 \\ 0 & 18 \end{pmatrix}$
$T_{(0,1,1)} = T_{(0,-1,1)}$	$\begin{pmatrix} 20 & 0 \\ 0 & -69 \end{pmatrix}$

Table 4 Hopping amplitudes within the two-orbital submanifold. Leading hopping processes $T_{(n_x, n_y, n_z)}$, where $\mathbf{r} = (n_x, n_y, n_z)$ identifies the bond connecting Co(1), see Fig. 2, to another cobalt at distance \mathbf{r} . The bonds emanating from Co(2) are obtained by the non-symmorphic symmetry, which, in particular, implies $n_z \rightarrow -n_z$. All hopping processes are written as matrices in the subspace (d_{xz}, d_{yz}) . The values, in meV, are obtained by the 5-orbital model restricted to the (d_{xz}, d_{yz}) subspace.